Design and characterization of a microchannel optical interconnect for optical backplanes

Yongsheng Liu, Brian Robertson, David V. Plant, H. Scott Hinton, and William M. Robertson

The design, modeling, and experimental characterization of a microchannel-based free-space optical interconnect is described. The microchannel interconnect was used to implement a representative portion of an optical backplane that was based on field-effect transistor, self-electro-optic device smart-pixel transceivers. Telecentric relays were used to form the optical interconnect, and two modes based on two different optical window clusterings were implemented. The optical system design, including the optical geometry for different degrees of clustering of windows supported by a lenslet relay and the image mapping associated with a free-space optical system, is described. A comparison of the optical beam properties at the device planes, including the spot size and power uniformity of the spot array, as well as the effects of clipping and misalignment for the different operating modes, is presented. In addition, the effects of beam clipping and misalignment for the different operating modes is presented. We show that microchannel free-space optical interconnects based on a window-clustering scheme significantly increase the connection density. A connection density of 2222 connections/cm^2 was achieved for this prototype system with 2×2 window clustering. © 1997 Optical Society of America

Key words: Microchannel free-space optical interconnects, optical backplane, optical design, optical window clustering, image mapping, optical system characterization.

1. Introduction

Free-space optical interconnects have several potential advantages for implementing highly parallel networks with large data bandwidths.[1] It has been shown that microchannel free-space optical interconnects that employ microlens arrays to relay optical beams relieve the constraints imposed by typical conventional macro-optic implementations.[2] The inherent problems associated with the limited numerical apertures and small fields of view of bulk relays are not significant factors in microchannel relays. In addition, the optical interconnect is unaffected by the angular dependence of polarizing beamsplitters (PBS's). Thus, microchannel relays can be made simple and compact, with a low component count, minimal latency, and high scalability.

Previous systems that demonstrated microchannel free-space optical interconnects by use of emitter-based devices have concentrated on only the implementation of optical relays in which each microchannel supports one connection.[2–4] This approach does not fully exploit the potential connection capacity of a microchannel optical interconnect. Recently, an optical backplane demonstrator based on field-effect transistor self-electro-optic device (FET-SEED) smart-pixel transceiver arrays was demonstrated.[5] This system used a microchannel optical interconnect to relay beams from a transmitter-printed circuit board to a receiver-printed circuit board. A window-clustering scheme in which multiple beams were relayed by a single lenslet relay was employed in the system. The interconnect was operated in two modes: In the first mode, the 2-clustered mode, a pair of optical beams representing one logical data channel were relayed through each lenslet relay. In the second mode, the (2×2)-clustered mode, eight optical beams representing four logical channels were supported by use of a single lenslet relay. The implementation of the clustered-window scheme permits a high intercon-

Y. Liu, B. Robertson, and D. V. Plant are with the Department of Electrical Engineering, McGill University, Montreal, Quebec H3A 2A7, Canada. H. S. Hinton is with the Department of Electrical and Computer Engineering, University of Colorado, Boulder, Boulder, Colorado 80309. W. M. Robertson is with the Department of Physics and Astronomy, Box X-116, Middle Tennessee University, Murfreesboro, Tennessee 37312.

Received 1 August 1996; revised manuscript received 27 November 1996.

0003-6935/97/143127-15$10.00/0

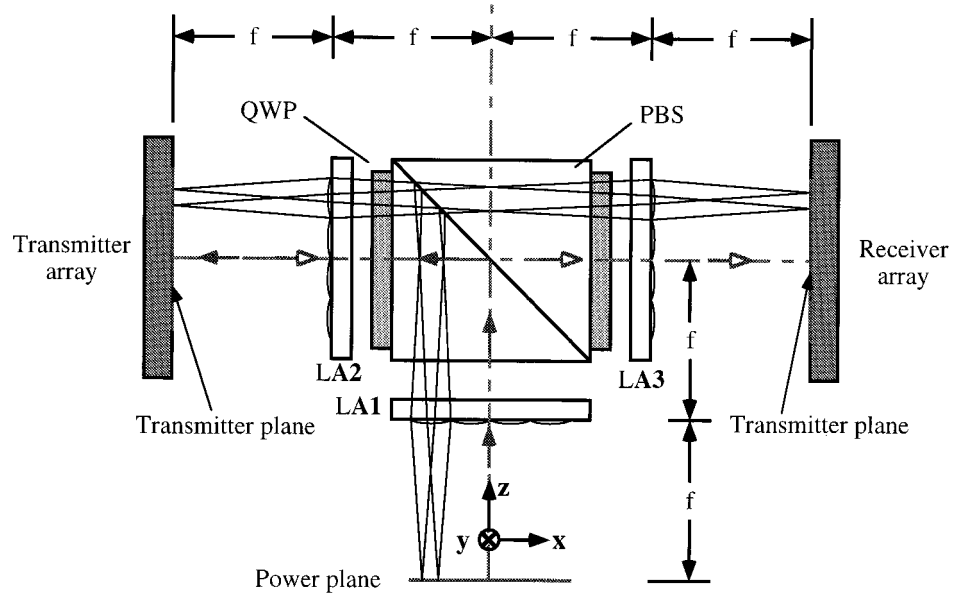

Fig. 1. Schematic of a unidirectional microchannel optical interconnect.

nection density and thus is attractive for free-space optical interconnects.[6,7]

This paper provides a detailed description of the design, modeling, and characterization of the optical interconnect used in this demonstrator system. In Section 2, we give the design of a clustered microchannel relay system using Gaussian beam propagation theory. The optical geometry, the degrees of clustering of the windows supported by a lenslet relay, and the image mapping associated with a microchannel free-space optical interconnect system are discussed. In Section 3, we provide a general outline of the optical system followed by a description of the two modes of operation of the backplane demonstrator. In Section 4, we characterize the key components used in the demonstrator, including the binary phase grating (BPG) used for spot-array generation and the diffractive lenslet arrays (DLA's) used for the microchannel relays. In Section 5, we present and compare the experimental performance of the optical system when operated in both modes and also compare those measurement results against the predicted performance. We conclude the paper with comments on the performance of the two modes operated in the backplane demonstrator.

2. Design of Microchannel Relays Based on Window Clustering

A. Optical Geometry with a Window-Clustering Scheme

Figure 1 shows the design of a microchannel optical interconnection. A simple Gaussian beam propagation model was used to analyze this interconnection geometry. The analysis assumed the following parameters: window size of an optical device of $d_w \times d_w$; window spacing of d_s; windows centered in the optical axis of the relay; the use of square-packed multilevel DLA's with apertures of $D_L \times D_L$. Here the term window is used for the aperture of the optical device. In addition, the aberrations, as well as the diffraction effects resulting from clipping the Gaussian beam by the finite dimension of the lenslets, were ignored.

Previous studies of microchannel optical interconnection geometries that employ microlens arrays have typically concentrated on interconnects in which a single optical beam is relayed along each microchannel.[2–4,8] The microchannel interconnects described here use a window-clustering scheme in which one lenslet relay supports multiple beams. Figure 2 illustrates a situation in which one lenslet supports two optical beams. It can be seen that the signal beams are focused at a distance d_y from the center of the pixel, where $d_y = d_s/2 + d_w/2$. Thus, as the interconnect is based on a telecentric relay, the maximum geometric beam radius r_d at the lenslet facet will be given by $r_d = D_L/2 - d_y$. To ensure that minimal clipping of the beam occurs as it propagates through the interconnect, we must restrict the

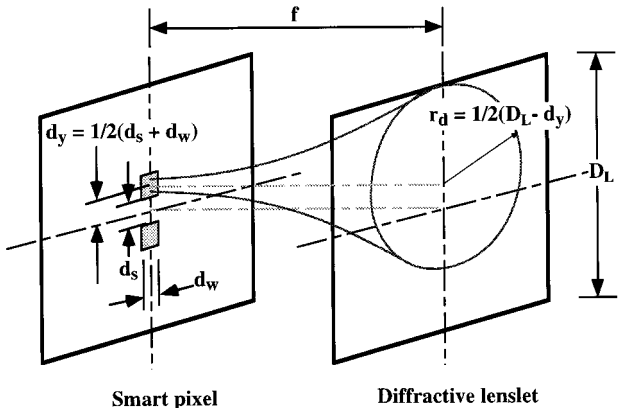

Fig. 2. Layout of one lenslet supporting two connections.

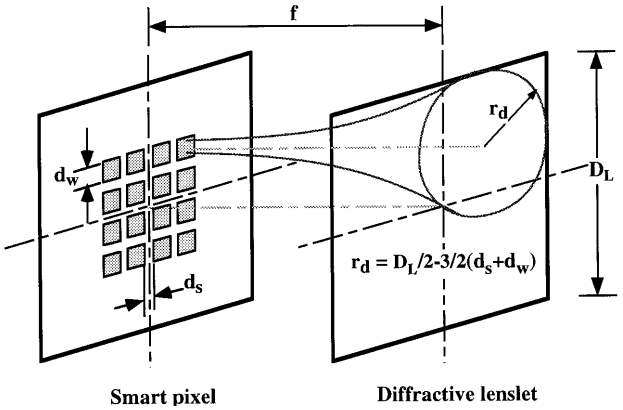

Fig. 3. Layout of one lenslet supporting 4 × 4 connections.

beam radius at the lenslet array. This is important, as clipping reduces the efficiency of the relay and can lead to increased levels of optical cross talk.[8,9] For the purposes of this analysis the limit $3\omega_L = 2r_d$ is used, where ω_L is the $1/e^2$ Gaussian beam radius of a signal beam at the lenslet array. This ensures that less than 1% of the light is lost. It therefore follows that

$$\omega_L = \tfrac{1}{3}[D_L - (d_s + d_w)]. \quad (1)$$

Similarly, at the device planes we impose the restriction that $3\omega_d = d_w$, where ω_d is the $1/e^2$ Gaussian beam radius of the focused beam. The beam radius at the lenslet array is given by standard Gaussian beam propagation theory:

$$\omega_L = \omega_d\left[1 + \left(\frac{f\lambda}{\pi\omega_d{}^2}\right)^2\right]^{1/2}. \quad (2)$$

The relations among window size, lenslet size, *f*-number of the lenslet, and the window density may all be derived from Eqs. (1) and (2).[8,10]

This analysis can be extended to the case in which the windows of the neighboring optical devices can be clustered together, and more windows can be supported by one lenslet. Figure 3 shows a case of a 4 × 4 array of clustered beams that are relayed by one lenslet. It can be seen that, for this arrangement, $r_d = D_L/2 - [(3/2)(d_s + d_w)]$. Thus, by applying the same clipping restrictions described above, we can calculate the corresponding dependence of connection density (defined as the number of connections per square centimeter) on the window size.

Figure 4 is a plot of the connection density versus the window size d_w as a function of the window spacing d_s. The window arrangement is that described in Figs. 2 and 3 for an interconnect of a focal length of $f = 6.25$ mm operating at 850 nm. This focal length was chosen to give a device-plane separation close to that used in current electrical backplanes (≈25 mm). Smaller window sizes result in Gaussian beams that diverge more rapidly, thereby requiring a larger lenslet facet to collect all the light. As a consequence, the connection density initially increases with window size. It can be seen from the plot [Fig. 4(b)] that, by use of a 4 × 4 clustered-window scheme, a connection density of 4000 connections/cm^2 may be obtained with parameters of $D_L = 632$ μm, $d_s = 30$ μm, $d_w = 35$ μm, and an angular field of view of 2.5°. These results indicate that one can increase the connection density significantly by clustering the windows of optical devices.

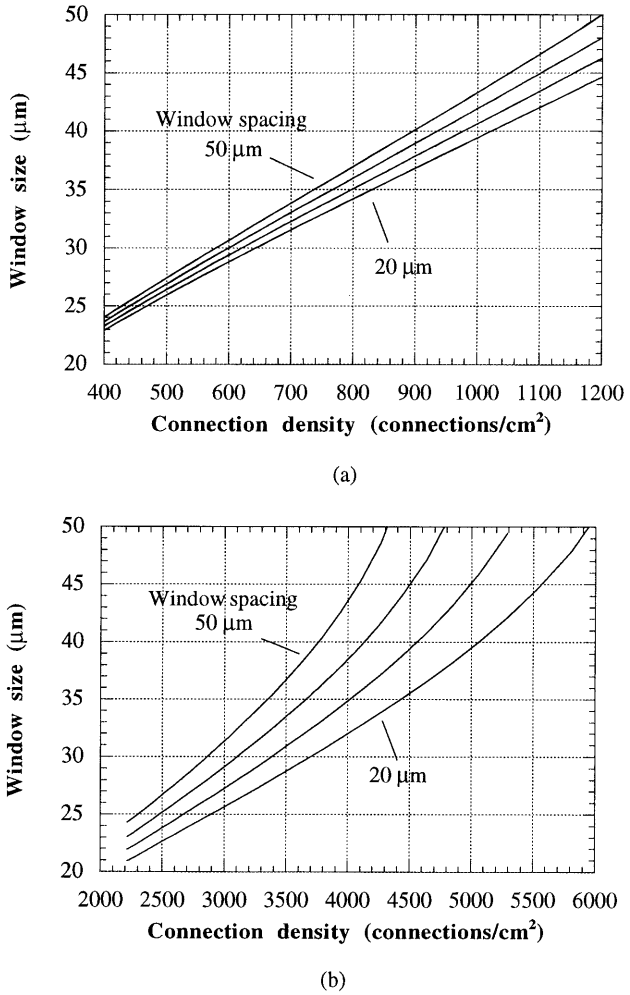

Fig. 4. Connection density with different window-clustering schemes: (a) for window clustering as shown in Fig. 2 and (b) for window clustering as shown in Fig. 3.

B. Image Mapping

In addition to defining the interconnection scheme, image mapping needs to be considered when designing a microchannel free-space optical interconnect based on a window-clustering scheme because of the complexities associated with signal routing. In particular, image mapping will affect the physical layout of the smart-pixel transceivers, which will further influence the architecture embedded in the optical system. In this subsection, we provide a general discussion of image mapping between the two devices.

For simplicity a matrix representation is used to show how the signal beams propagate through the optical interconnect. The coordinate system is cho-

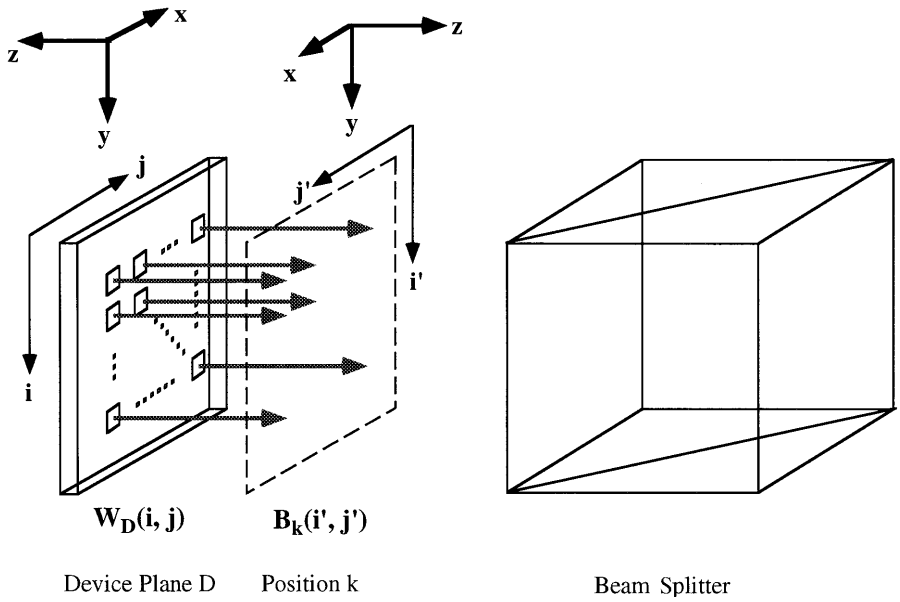

Fig. 5. Coordinate system for image mapping.

sen such that the z axis is always pointed in the same direction as the beams are propagating (therefore it changes its direction as the beams are deviated), and the x–y–z axes form a right-hand Cartesian coordinate system. For this analysis, the y axis is chosen to be parallel to the reflection surface of a beam splitter, as shown in Fig. 5.

Standard matrix notation $B_k(i, j)$ is used to represent the array of optical beams at position k when it is observed along the z axis, and $W_D(i, j)$ is used to represent the array of optical windows at device plane D. Note that a change of the coordinate system will affect the notation for a specific array of beams. For instance, an $M \times N$ array of beams from the array of windows $W_D(i, j)$ of an optical device is represented as $B_k(i, N - j + 1)$ instead of $B_k(i, j)$, if the same i and j are used, since the coordinate system is changed from one in which the z axis is opposite to the propagation direction of the optical beams at the device plane D to one in which the z axis is along the propagating direction of the optical beams at position k. For convenience, the change of notation resulting from the change of the coordinate system is also regarded as image mapping. In general, the permutation of the signal beams with respect to the coordinate system is as follows:

- An $M \times N$ array of beams $B(i, j)$ propagating through a telecentric relay system will be inverted to $B(M - i + 1, N - j + 1)$, if it is assumed that the beams are centered with respect to the optical axis.
- An $M \times N$ array of beams $B(i, j)$ reflected from a mirror will be transformed to $B(i, N - j + 1)$, if it is assumed that the surface of the mirror is parallel to the y axis.

Image mapping will become more complex if a window-clustering scheme is used to increase the connection density. When the clustered-beam array is relayed by a telecentric relay, an image inversion will occur within each group of clustered beams supported by a lenslet relay. However, when the beam array is reflected by a mirror (or when the coordinate system is changed), image mapping occurs across the entire array of beams. For example, Fig. 6 shows an optical interconnection system consisting of two, 2×2 lenslet arrays with each lenslet supporting 4×4 clusters of windows. The optical windows at the transmitter plane can be represented as $W_T(i, j)$. Because of the change in the coordinate system from one in which the z axis is opposite to the propagation direction of the optical beams to one in which the z axis is along the direction of signal-beam propagation, the beam array leaving the transmitter array will be written as $B_T[i, 2(4 - j) + 1]$ if the same index (i, j) is used. However, on the receiver side, there is no change in the coordinate system; therefore there is no need to change the notation in the matrices $B_R(k, l)$ and $W_R(k, l)$. It is noted that the image mapping of each group of 4×4 beams is relative to the optical axis of the lenslet relay that supports the 4×4 beams. There is no image mapping between the groups. By applying the mapping rule for a telecentric relay to each group, we can express the image mapping between the beams $B_T[i, 2(4 - j) + 1]$ and $B_R(k, l)$ as

$$k = \begin{cases} 4 - i + 1 & i \le 4 \\ 13 - i & 4 < i \le 8' \end{cases}$$
$$l = \begin{cases} 4 + j & j \le 4 \\ j - 4 & 4 < j \le 8 \end{cases}. \quad (3)$$

Therefore, the optical beams from windows $W_T(i, j)$ of the transmitter array are mapped into the windows

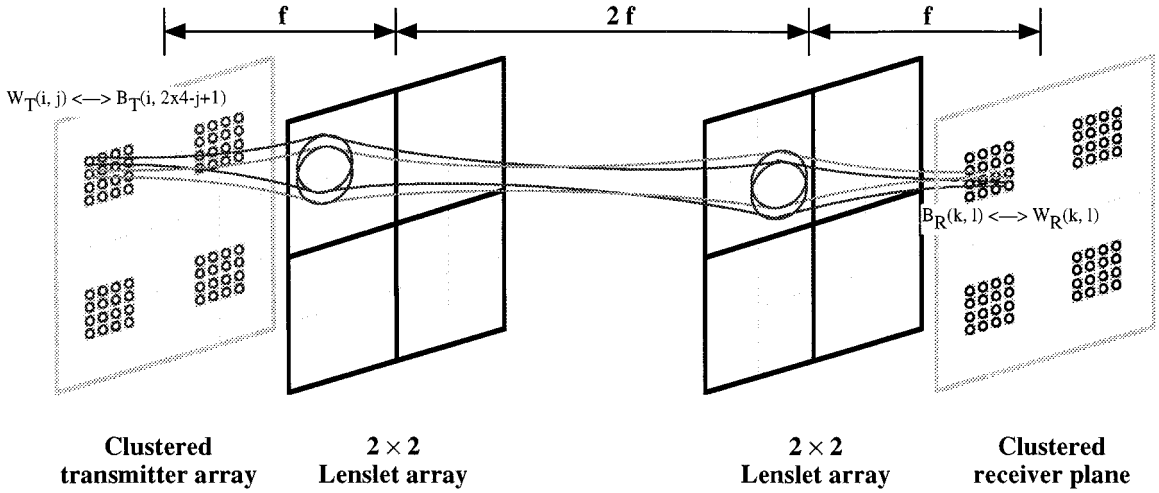

Fig. 6. Optical layout for image mapping between the beams from clustered transceiver arrays.

$W_R(k, l)$ of the receiver array according to the relations in Eqs. (3).

Imaging mapping is important not only with respect to the design of an optical interconnect but also for laying out smart-pixel transceivers. In Section 3 we present a description of a system built using a window-clustering scheme.

3. Microchannel Optical System for a Backplane Demonstrator

Figure 7 is a schematic of a microchannel free-space optical backplane system that employed DLA's and FET-SEED smart-pixel transceiver arrays. Figure 8 is a photograph of the system. The design of the

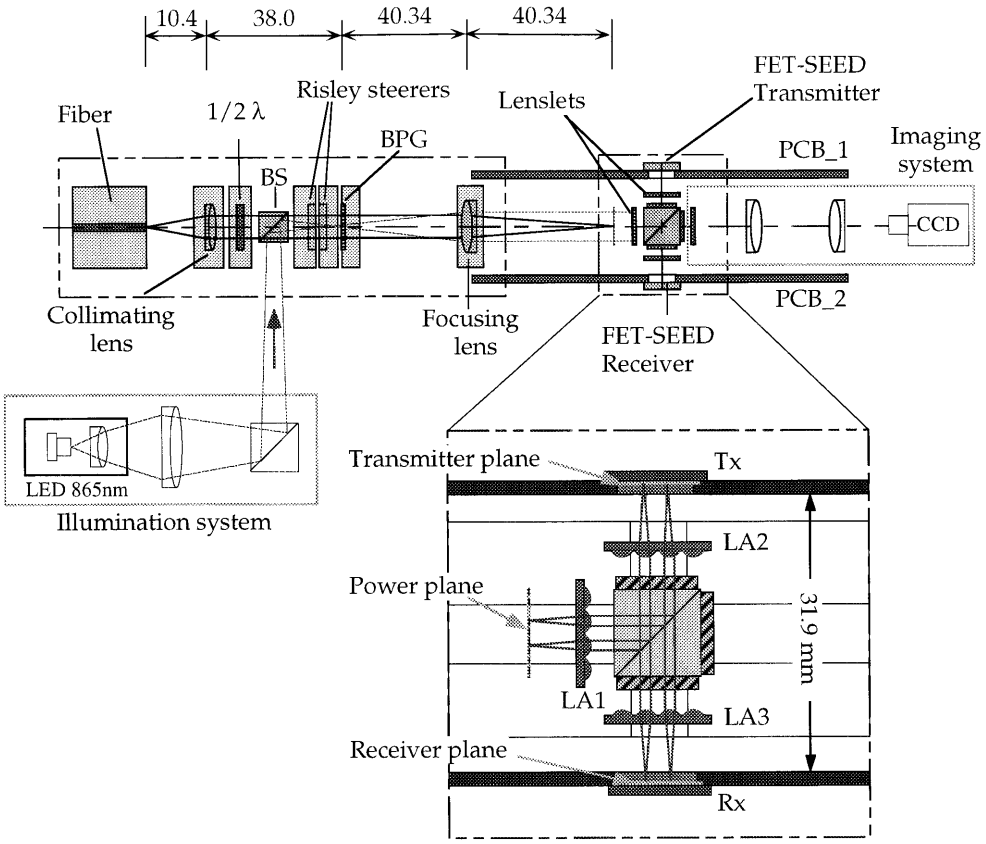

Fig. 7. Schematic of the optical system used in the backplane demonstrator. PCB_1 and PCB_2 are the print circuit boards where the FET-SEED transmitter and FET-SEED receiver were mounted, respectively.

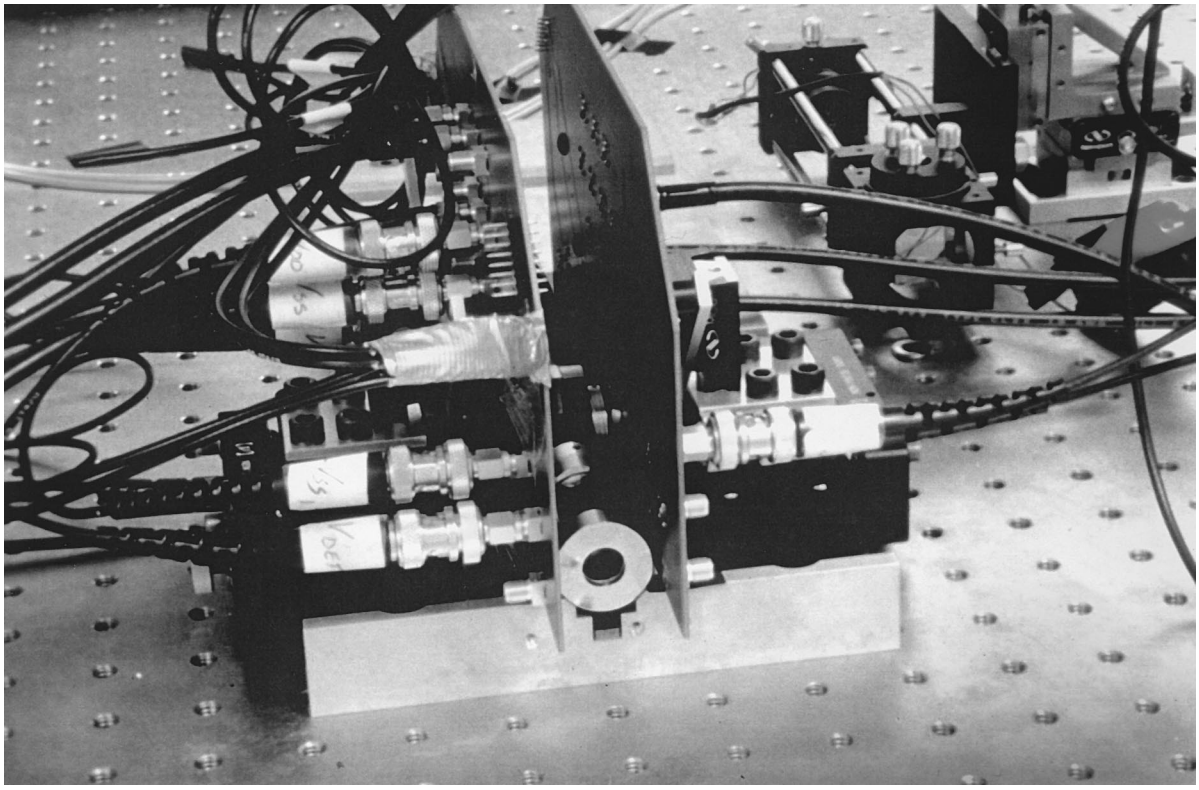

Fig. 8. Photograph of the demonstrator system.

optical system was divided into three discrete subsystems: the optical power supply, which generated an array of beams at the power plane; the microchannel optical interconnect system, which relayed the optical beams from the power plane to the transmitter plane and the subsequently modulated signal beams to the receiver plane; and the illumination and imaging system, which provided a direct way to monitor the system during assembly. In this section we present a description of the design of these subsystems.

In the optical power-supply subsystem, 850-nm light from a Ti:Sapphire laser was coupled into a polarization-maintaining single-mode fiber. The output beam from the fiber was collimated by use of a 10.41-mm focal length doublet lens. The collimated beam was then diffracted by a BPG and focused by a 40.34-mm focal length doublet lens to form an 8×4 spot array at the power plane, as shown in Fig. 9. The pitch of the spot pairs was 200 μm and the separation of the spots in a pair was 50 μm. A half-wave plate was used to ensure the optical beams from the optical power supply were *s* polarized. Risley steerers were used to achieve fine positioning of the optical beams.

In the illumination and imaging subsystem, the illuminating beam was produced by a 865-nm light-emitting diode (LED) and was directed into the optical system by means of a beam splitter (BS), as shown in Fig. 7. The illuminating beam followed the same optical path as the signal beam and illuminated the transmitter and receiver planes. A CCD camera was used to capture the images of the signal spot arrays on the transceiver devices at these two planes.

In the microchannel optical interconnect subsystem, the optical interconnects were built by use of three, eight-phase-level DLA's that formed two telecentric

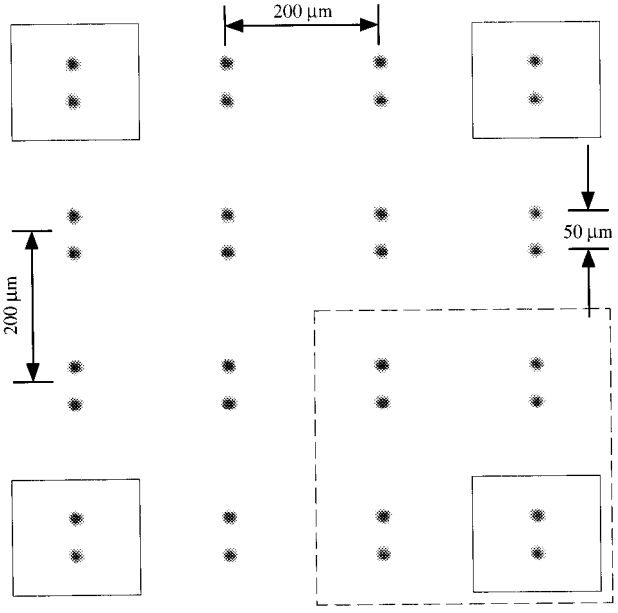

Fig. 9. Spot array generated at the power plane. The optical beams in the solid-line boxes were used for the interconnection in the 2-clustered mode, and the beams in the dashed-line box were used for the (2×2)-clustered mode.

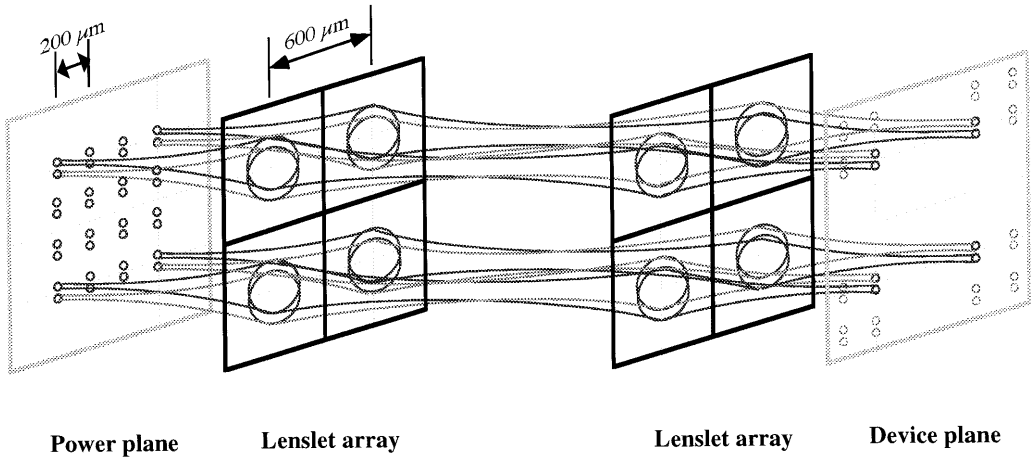

Fig. 10. Schematic of the 2-clustered mode in which optical beams were relayed from the power plane to the transmitter plane.

optical relays, as shown in Fig. 1. The first telecentric optical relay was set up between the power plane and the transmitter plane by use of lenslet arrays LA1 and LA2. The second telecentric relay was set up between the transmitter plane and the receiver plane by use of lenslet arrays LA2 and LA3. The center-to-center distance of the lenslets in the DLA's was 600 μm, and the focal length of the lenslets was 6.5 mm. The PBS and quarter-wave plate (QWP) assembly (PBS + QWP) was used to direct the optical beams from the power plane to the transmitter plane and then to route the modulated signal beams from the transmitter plane to the receiver plane. The FET-SEED transceiver chips consisted of an individually addressable 4 × 4 transmitter array and an individually addressable 4 × 4 receiver array. The FET-SEED's were configured to operate in a differential logic mode, thus requiring a dual-rail optical encoding scheme for data transmission. Therefore, each transmitter and receiver was constructed with two SEED devices. Each SEED window was 25 μm × 25 μm, and the gap between windows was 25 μm. The pitch of the window pairs in the transmitter and the receiver arrays was 200 μm in both the horizontal and vertical directions.[11,12]

On the basis of the pitch of the DLA's (600 μm) and the FET-SEED transceivers (200 μm), the prototype system was designed to operate in the 2-clustered mode, as shown in Fig. 10. Here, the four corner transmitters were optically connected to the four corner receivers, and each lenslet relay supported two optical beams or one logical channel. The criteria for clipping in this design, however, was set at $2.6\omega_0 = d_w$ for the Gaussian beam on a device window and $3\omega_L = 2r_d$ for the Gaussian beam on a lenslet facet. The Gaussian beam spot size on the device plane was calculated to be 9.6 μm.

In addition to the above mode and because the device array pitch was smaller than the lenslet array pitch, it was possible to have the optical system operate in a (2 × 2)-clustered mode. A 2 × 2 subset of transceivers were optically connected. Each lenslet relay, in this case, supported eight optical beams forming four logical channels. In the remaining part of this section, we describe in detail the calculated performances of both of these modes of operation of the system.

A. 2-Clustered Mode

Starting from the fiber output, the mode-field diameter of the single-mode fiber at 850 nm was measured to be 5.0 μm. Assuming the output beam from the single-mode fiber was a Gaussian beam, the focused spot size ($1/e^2$ beam diameter) of the spot array at the power array was calculated to be 19.4 μm by use of the ABCD law. Since the lenslet relays from the power plane to the transmitter plane and the transmitter plane to the receiver plane were both in a 4*f* configuration, the Gaussian beam spot sizes were theoretically identical at both the transmitter and receiver planes. The effective aperture of each lenslet was 3.26 times larger than the Gaussian beam diameter on the facet of the lenslet, therefore diffraction effects caused by a finite aperture were neglected.[12,15,16]

In addition to Gaussian beam propagation theory, ray tracing was also used to estimate the geometric aberrations of the optical system to determine the focal lengths and the apertures of the lenses used in the system and to optimize the locations of the optical components. Ray tracing was performed by use of a

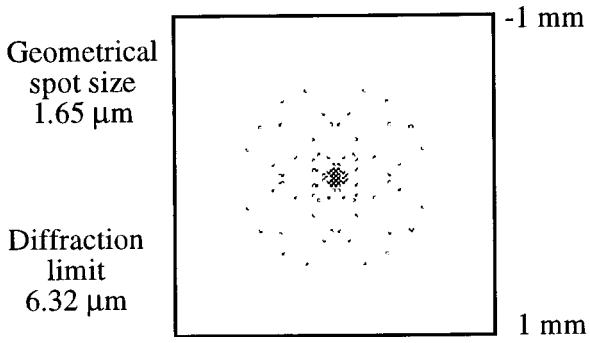

Fig. 11. Geometrical spot diagram at the power plane.

commercial ray-tracing program—OSLO SIX—from Sinclair Optics. For simplifying the ray-tracing process, the BPG was modeled as a grating in which the pitch and order were matched to the spatial order of the array of spots at the power plane. The diffractive lenslet was modeled as a very-high-index thin lens by use of Sweatt's hologram model.[15,16] For simulating the Gaussian beam propagation in the optical system when performing a ray trace, the Gaussian apodized pupil function was used to weight the rays. As is shown in Fig. 10, only the spot pairs close to the optical axis of each lenslet were relayed to the active windows on the device planes without being clipped by the lenslets. Since these spot pairs were close to the optical axis, the geometric aberrations were negligible. The remaining spot pairs from the BPG were severely clipped and aberrated by the lenslet array because they were well off axis. However, as the interconnect was not designed to route those beams, they are not further discussed in this paper. Figure 11 shows a geometric spot diagram at the power plane. The overall spot sizes at the transmitter and receiver planes were calculated by use of Gaussian beam theory. The rms spot size was approximately 1.7 μm; therefore, the overall spot size, to a first approximation, was $(1.7^2 + 19.4^2)^{1/2} = 19.5$ μm.

The optical system was designed for maximum optical power throughput between transmitter and receiver arrays. The optical power throughput η for a Gaussian beam passing through a square aperture can be expressed as

$$\eta = \frac{1}{4}\left\{\mathrm{erf}\left[\frac{\sqrt{2}}{\omega}\left(\frac{a}{2} - \delta_x\right)\right] + \mathrm{erf}\left[\frac{\sqrt{2}}{\omega}\left(\frac{a}{2} + \delta_x\right)\right]\right\} \times \left\{\mathrm{erf}\left[\frac{\sqrt{2}}{\omega}\left(\frac{b}{2} - \delta_y\right)\right] + \mathrm{erf}\left[\frac{\sqrt{2}}{\omega}\left(\frac{b}{2} + \delta_y\right)\right]\right\}, \quad (4)$$

where a and b are the dimensions of the aperture, δ_x and δ_y are the offsets of the beam waist to the center of the aperture, ω is the beam waist on the facet of the lenslet, and erf is the error function, defined as

$$\mathrm{erf}(x) = \frac{2}{\sqrt{2}}\int_0^x e^{-t^2}\mathrm{d}t. \quad (5)$$

With this formula, the overall power throughput can be calculated as the beam propagates through the system. When all the components in the system were perfectly aligned, the power loss that is due to clipping from the lenslets and the device windows was estimated to be 8%.

Figure 12 shows the optical power budget for the microchannel optical system. The power budget did not include the power loss resulting from misalignment, clipping effects, or aberrations in the system. It considers only the reflection losses of the optical components and efficiencies of the diffractive components. It can be seen that the largest power loss within the system was due to the low reflectivity of the multiple-quantum-well transmitter devices (only 30% for the low absorption state and 15% for the high absorption state).

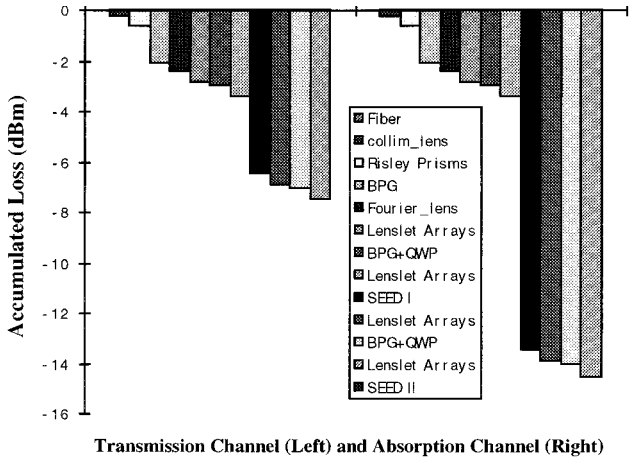

Fig. 12. Optical power budget for the microchannel optical system operated in the 2-clustered mode.

The allowable alignment tolerance was estimated on the basis of the on-axis Gaussian beam propagation theory. Table 1 shows the alignment tolerances for the 2-clustered mode. The mechanical tolerances for each optical component were obtained for a specific misalignment by calculation of the maximum allowable displacement required to produce a 5% drop in power throughput. Hence, the total allowable loss resulting from the maximum offsets of all six optical parameters was 30%. Here the combined effects of these offsets were not included. It should be noted that the maximum allowable rotation for the device planes will be drastically reduced if the size of the transceiver is increased. Although the estimated alignment tolerance did not include aberrations and diffraction effects (caused by the finite dimension of the lenslets), it provided a guideline for the alignment accuracy of the optical system. The relatively large allowable misalignments associated with the separation between the lenslet arrays and

Table 1. Alignment Tolerance for the 2-Clustered Mode

Parameters	Allowable Misalignment
Source	
Spot separation	±0.25%
Lateral Position	±5 μm
Wavelength	±1 nm
Lenslet array	
Lateral offset	±10 μm
Longitudinal offset	±25 μm
Tilt and rotation	±2°
Devices	
Lateral offset	±1 μm
Longitudinal offset	±25 μm
Tilt and rotation	±0.25°

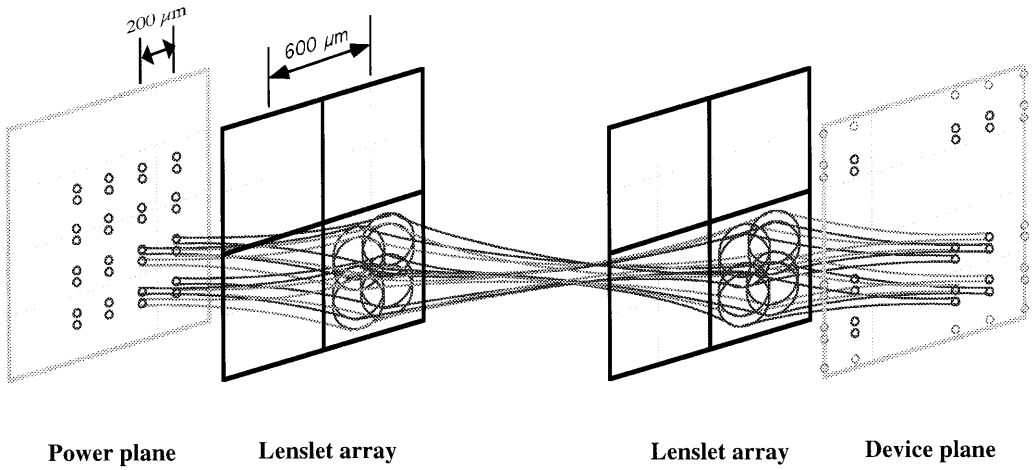

Fig. 13. Schematic of the (2 × 2)-clustered mode in which optical beams were relayed from the power plane to the transmitter plane.

the device planes were due to the large *f*-number of the lenslets (>$f/10$) used in the optical system. However, it was observed that the efficiency was far less dependent on the misalignment of the lenslets than that of the device planes.

B. (2 × 2)-Clustered Mode

Although the prototype optical system was primarily designed to operate in the 2-clustered mode, it could also be operated in the (2 × 2)-clustered mode because the device array pitch was smaller than the lenslet array pitch. It was noted, however, that the optical performance was degraded accordingly since the optical system was not optimized to operate in this mode. Figure 13 shows the (2 × 2)-clustered mode for the optical relay from the power plane to the transmitter plane, in which one lenslet supported eight optical beams representing four data channels (as shown within the dashed-line box in Fig. 9).

The same type of relay was used to interconnect the modulated beams from the transmitter plane to the receiver plane. It can be seen that each spot from the power array plane was altered not only by the diffraction effects of a finite dimension of the lenslet but also by the aberrations arising from the off-axis locations of the spot array. The $1/e^2$ beam radius on the lenslet was approximately 184 μm, thus the clipping ratio (defined as the effective aperture divided by 2 times the beam waist) was only 2.2. As a result of this low clipping ratio, significant diffraction occurred as the beam propagated; this altered the beam characteristics, hence the weak clipping approximation for the Gaussian beam was no longer valid.[17] Therefore, an analysis based on rigorous diffraction theory would be necessary, but is not presented in this paper because of the considerable modeling required for a very specific system. It was also noted that the diffraction effects caused optical cross talk between the channels, and thus the data rate for each channel had to be reduced to maintain the same quality signal as the 2-clustered window interconnect.

For estimating the alignment tolerance of the (2 × 2)-clustered mode with respect to the 2-clustered mode, the Gaussian beam propagation model was assumed valid, even though the clipping ratio was 2.2. This was done to allow some measure of the performance to be obtained analytically without the need for enormous amounts of computation. Diffraction effects were neglected, and the optical beams were assumed to remain Gaussian. The alignment-tolerance analysis for the clustered mode was similar to that of the 2-clustered mode because both optical systems consisted of telecentric relays. The main difference was that the maximum power throughput was reduced to 50.0% with respect to the 2-clustered mode as a result of the large clipping losses that occurred when the beams passed through the lenslets.

Because the (2 × 2)-clustered beams were significantly off axis, some of the maximum misalignment tolerances had to be reduced. These were calculated in a manner similar to that of the 2-clustered mode. For instance, the lateral offset of the optical spots at the power plane had to be within ±3.5 μm, and the tilt angle of the incident beams at the power plane had to be less than 0.2°. It was also found that rotation of the microlens arrays with respect to each other caused a very significant power loss arising from clipping. As a result, the rotational offset of the lenslet arrays had to be controlled to within ±1.5°.

When diffraction effects were taken into account, the maximum allowable misalignment of the components became even smaller because, when the Gaussian beam was diffracted, it focused to a spot that was closer to the lens and diverged a greater rate,[18] as shown in Fig. 14. Thus, the second lens in the relay received even less light than expected, and an additional power loss resulted.

The geometric spot size estimated by ray tracing in the clustered mode did not increase significantly. This may result from the limitation of the hologram model for the diffractive lenslets. A more rigorous model that takes into account the off-axis aberrations

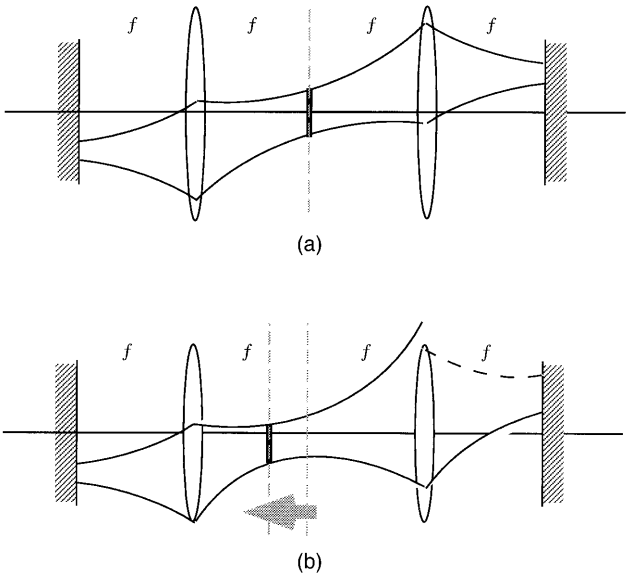

Fig. 14. Schematic of the "pull" effect for the beam waist when the diffraction effects resulting from clipping were taken into account. (a) Off-axis Gaussian beam without diffraction effects. (b) Off-axis Gaussian beam with diffraction effects, showing a minimum spot size closer to the first lens.

of the diffractive lens is required for a more detailed analysis.

Since the prototype optical system was not optimized for operation in the (2×2)-clustered mode, the optical performance did not prove to be good. It can be shown, however, that an optical system that employs a window-clustering scheme has advantages of not only high connection density[7] but also improved alignment tolerance. The optimal design of the optical interconnect results from the trade-off between the connection density and the maximum data rate for each connection.

4. Optical Performance of Diffractive Optics

The optical interconnect was constructed by use of two custom diffractive optical components, a BPG, and three, eight-phase-level diffractive lenslet arrays. In this section, we describe the design and associated performance of these components.

A. Binary Phase Grating

The periodical structure of the BPG used in the system was a nonseparable type[19] that was optimized by use of a simulated annealing algorithm.[20] The period was 1.37 mm in both the x and y directions and contained 128×128 pixels. Note that, as only two quantization levels were used, the inherent efficiency for the fan-out grating was low. In addition, antireflection (AR) coatings were not used, which accounted for an additional 7.8% of reflection loss.

The number of periods on the BPG that are sampled, or illuminated, by the input collimated beam affects the power uniformity of the spot array generated at the power plane. The number of the periods sampled, NPS, is defined as $\mathrm{NPS} = 2\omega_{\mathrm{BPG}}/P$. Here

Table 2. Spot Power Uniformity of the BFG versus the NPS

	NPS		
	1.7	4.1	6.5
Uniformity	86.3%	92.5%	94.0%

ω_{BPG} is the Gaussian beam waist on the BPG and P is the period in the BPG. As the NPS is reduced, the uniformity degenerates. Another common parameter used to describe the NPS is the compression ratio, CR, defined as $\mathrm{CR} = S/3\omega_{\mathrm{pwr}}$. Here S is the minimum spot separation at the power plane and ω_{pwr} is the spot size at the power plane. According to standard Gaussian beam propagation theory, we have

$$\omega_{\mathrm{pwr}} = \frac{f\lambda}{\pi\omega_{\mathrm{BPG}}}. \tag{6}$$

Here f is the focal length of the focusing lens. The relation between the spot separation at the power plane S and the period in the BPG P is[21]

$$S = \frac{2f\lambda}{P}. \tag{7}$$

The factor of 2 in Eq. (7) is due to the fact that only even-numbered spots were generated by the BPG. From Eqs. (6) and (7) and the definitions of NPS and CR, the relation between CR and NPS can be found as

$$\mathrm{CR} = \frac{\pi}{3}\,\mathrm{NPS}. \tag{8}$$

For an optical interconnect system with good power uniformity, it was believed that $\mathrm{CR} > 3$ ($\mathrm{NPS} = 2.86$) would be required to reduce the nonuniformity resulting from aliasing.[22] Table 2 shows the measured power uniformity for three cases of sampling. The power uniformity was calculated by use of $1 - (P_{\max} - P_{\min})/P_{\mathrm{ave}}$. Here, $P_{\max}$, $P_{\min}$, and P_{ave} were the maximum, minimum, and average powers, respectively, of the spots of the array produced by the BPG. In our optical system, the NPS of 1.7 ($\mathrm{CR} = 1.78$) provided a reasonably uniform spot array (86.3%) at the power plane. It is very important to determine the smallest NPS for a desired power uniformity for a given optical system. A small NPS corresponds to a small beam diameter, which reduces some of the constraints on the optical components used in the system. For example, the required field of view of the lenses in the system can be reduced. Therefore the optical system can use cheap and simple components, and the system can be compact. It was noted that the spot uniformity also depended strongly on the incident-beam properties. Poor beam collimation or a collimated beam incident at small angle with respect to the grating strongly affected the power uniformity of the spot array at the power plane. Different optimization processes may also affect the power uniformity.

The power efficiency for a value of NPS = 6.5 was measured to be 67.4%. This result was obtained by summation of the powers of the individual spots generated and division of the power of the incident optical beam. Considering the optical power loss that is due to the reflection of the glass substrate of the BPG, the diffraction efficiency of the BPG was calculated to be 73%.

B. Diffractive Lenslet Arrays

The eight-phase-level square diffractive lenslet arrays were fabricated on a fused silica substrate with a designed focal length of 6.5 mm and a pitch of 600 μm. There was an AR coating on the back surface of the etched substrate. The *f*-number was 10.8 (defined as the focal length divided by the diameter of the largest circle inscribed within the square lenslet). The theoretical diffraction efficiency is 95.0% for an eight-phase-level diffractive lenslet.[23] Measurements showed that the lenslet array was diffraction limited and had a total power efficiency, defined as the optical power of the first-order diffracted beam divided by the power of the incident beam, of 90.0%. Taking the reflection loss (4%) at the front surface (no AR coating) of the lenslet into account, the diffraction efficiency of the lenslet array was calculated to be 93.7%, which is close to the theoretical limit. Since the lenslet had a large *f*-number, it was insensitive to variation in the incident-beam angle. For an incident angle within ±6° of the normal, the diffraction efficiency was within 98% of the maximum efficiency. The focal length across the lenslet array was measured to be 6.510 mm ± 13 μm. The variation of the focal length was due to the uncertainty in measuring the focal positions, because the lenslets were very slow thus the depth of focus was long.

5. Optical System Characterization

In this section, we describe the performance of the complete optical interconnect and compare the measured results to the predicted performance. As is shown in Fig. 8, the optical system was constructed on a magnetized slotted baseplate to reduce misalignment and drift.[24] With reference to Fig. 7, the optical fiber, collimating lens, half-wave plate, Risley beam-steering prisms, and focusing lens were mounted in standard 1-in.-diameter holders and prealigned to within ±10 μm of the optical axis. The PBS + QWP assembly was aligned in the baseplate by use of a pedestal arrangement, with which the tilt and rotation were controlled to better than ±0.2° with respect to the optical axis. LA1 was mounted in a single holder 6.5 mm from the power plane (where the initial spot array was generated). LA2 and LA3 were mounted in a custom-designed optomechanical steel bracket that could mechanically hold both lenslet arrays parallel to each other but positioned such that they were on opposite sides of the PBS. The separation error between LA2 and LA3 was controlled to within ±50 μm, and the centers of the lenslet arrays were positioned to within ±5 μm with respect to the optical axis. The relative rotation of the LA3 with respect to LA2 was measured to be less than 1°.

The characterization of the optical system was performed at the three locations at which the signal beams were focused. These were the *power* plane, the *transmitter* plane, and the *receiver* plane. For this application, the main concern was the optical power incident on the transceivers. The quality of the optical beams at these points in the relay was of less concern as long as the largest percentage of power was incident on the transceiver. This criterion differed from conventional optical system characterization in which standard characterizations such as the modulation transfer function of the optical system are required. In this system, the spot sizes and spot uniformity, as well as power levels, of the spots at the above three planes were of primary concern. Spot-size measurements were carried out with a high-resolution CCD camera that was calibrated by a scanning-slit beam profiler having a measurement accuracy of 0.01 μm. In addition, the automatic gain control of the CCD camera was not used so that the exact relative powers could be measured. Finally, the glass cover plate in front of the CCD sensor chip was removed to avoid the effects of the multiple reflections caused by this component.

A. Spot Array at the Power Plane

The collimated beam diameter ($1/e^2$ diameter, assuming a Gaussian profile) at the position of the BPG was measured to be 2.25 mm and had a 97% fit to an ideal Gaussian beam; therefore, the number of periods of the BPG sampled was approximately 1.66. The small number of periods sampled and the finite size of the individual pixels on the BPG caused power variations across the spot array. However, the small diameter of the incident collimating beam also reduced the constraints of the optical components, such as the fields of view of the lenses used in the system. The power uniformity across the entire 32-spot array was measured to be approximately 86.3%. For the spots in the 2-clustered mode (the spots in the solid-line boxes in Fig. 9), the power uniformity was measured to be 94%, whereas for the spots in the (2 × 2)-clustered mode (the eight spots in the dashed-line box in Fig. 9) the power uniformity dropped to 87%. The difference in uniformity may have been caused by the diffraction pattern of the individual pixels in the BPG. Since each pixel followed the sinc^2 function for its diffraction pattern, the middle of the sinc^2 intensity modulated the entire output spot pattern, causing it to roll off toward the edges by a few percent.

The spot separations were obtained with a CCD camera that was calibrated with a high-resolution Ronchi reticle. The measurements showed that the average separation between the spot pairs was 50.5 ± 0.1 μm and the pitch of the spot pairs was 203.1 ± 0.8 μm. The pitch of the spot array was determined by the focal length of the focusing lens and the period of the BPG. If we assume that the period of the BPG is exact, then the focal length of the Fourier lens can be found according to Eq. (5). From

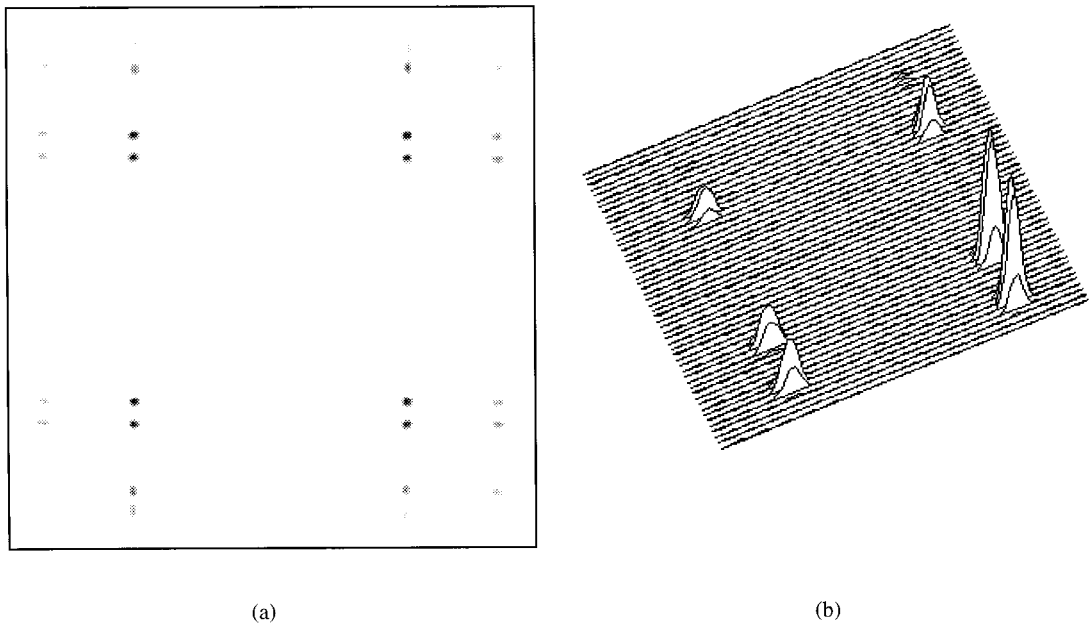

(a) (b)

Fig. 15. Optical spots at the transmitter plane for the 2-clustered mode: (a) spot pattern and (b) 3-D plot of the upper-left portion of spots.

these measurements the focal length of the focusing lens was estimated at 40.73 ± 0.08 mm. The error in focal length was approximately 0.7%, which was not within the specified tolerance for this system. Normally the specified focal-length error of off-the-shelf lenses is within 2%; thus, to have an exact focal length with commercial lenses, we combined a pair of lenses in a Petzval mode. For two lenses with focal lengths f_1 and f_2 the combined focal length can be expressed as $f = f_1 f_2/(f_1 + f_2 - d_{Hb_1-Hf_2})$, where $d_{Hb_1-Hf_2}$ is the distance between the back principal point of the first lens and front principal point of the second lens. By adjusting the separation between the two lenses, one can achieve an accurate focal length, hence the correct spot separation. The spot size on the power plane was measured to be 19.8 ± 0.3 μm, which was slightly larger than the design value of 19.5 μm. This may have been due to the difference between the ideal Gaussian beam and the real optical beam, as well as the misalignment in the optical power supply.

B. Spot Array at the Transmitter Plane

Figure 15(a) shows the spot pattern of the 2-clustered mode at the transmitter plane, and Fig. 15(b) shows a three-dimensional (3-D) plot of the upper-left portion of the spot array. The power uniformity at the transmitter plane was 94%. It can be seen from Fig. 15(b) that the intensity of the clipped beams was much lower (by at least 0.38 dB) than that of those in the center. The farther the spots were from the optical axis, the stronger the clipping effects and aberrations, and the less the amount of optical power that reached the device planes. Figure 16(a) shows the spot pattern of the (2 × 2)-clustered mode at the transmitter plane, and Fig. 16(b) shows the 3-D plot of the (2 × 2)-clustered spots. It was noted that the spot patterns of Figs. 16 were different from that of Fig. 13. This was due to an additional image mapping by the reflection surface of the PBS + QWP, as was discussed in Section 2. The uniformity of the (2 × 2)-clustered spots was 72%. The degradation of the power uniformity in the (2 × 2)-clustered mode was caused by the combined effects of the nonuniformity of the spot array in the power plane and the strong diffraction effects introduced by the lenslet arrays.

The spot size on the transmitter plane was measured to be 19.8 ± 0.6 μm for the 2-clustered mode. The variation in the spot size in the 2-clustered mode was small, and the sizes of the spots were only slightly enlarged compared with the spot sizes at the power plane. In contrast, the average spot size was 22.6 μm for the (2 × 2)-clustered mode, approximately a 2.8-μm increase compared with the spots at the power plane. This enlargement of the spot size was due to the combined clipping effect and misalignment. Table 3 shows the spot sizes for the (2 × 2)-clustered spot array in the transmitter plane. The uniformity of the spot size was 88.9%. These measurements showed that clipping effects and misalignment not only reduced the power efficiency and power uniformity of the spots across the array but also increased the spot sizes and variation of the spot sizes across the array. Moreover, the spots on the transmitter plane showed strong astigmatism.

C. Spot Array at the Receiver Plane

Initially, we measured the spot array at the receiver plane by replacing the transmitter array with a mirror that had $R > 96\%$ reflectivity. This was done to quantify accurately the interconnect independently of the transceiver technology. Figure 17 shows the optical spots on the receiver plane for the 2-clustered

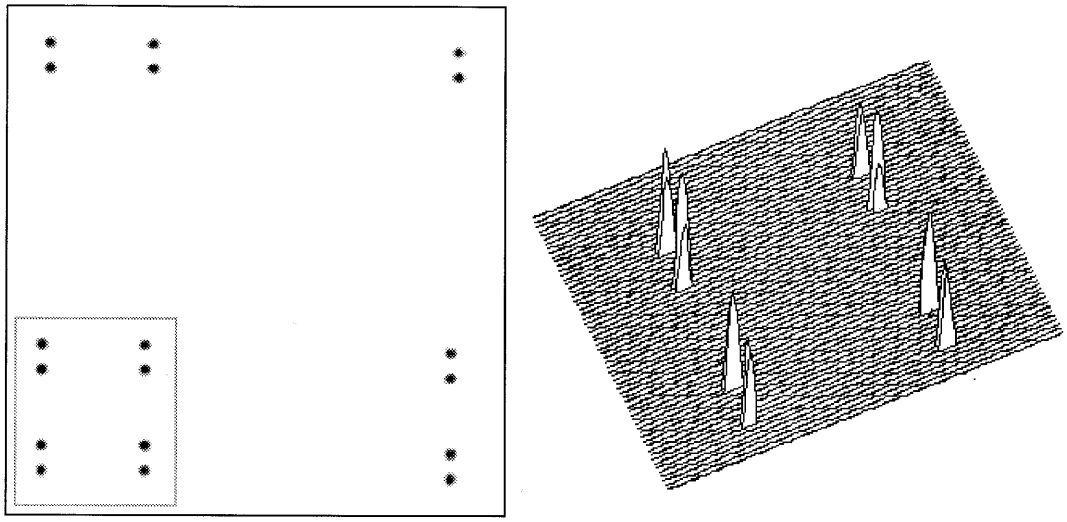

(a) (b)

Fig. 16. Optical spots at the transmitter plane for the (2 × 2)-clustered mode: (a) spot pattern and (b) 3-D plot of the (2 × 2)-clustered spots shown in the box.

mode. Because of accumulated clipping effects and misalignment in the optical system, the power uniformity of the spots in the 2-clustered mode degraded to 85.3%. In the (2 × 2)-clustered mode, the optical beams were further deteriorated by the combined effects of clipping, misalignment, and aberrations, and the power uniformity of the spots on the receiver plane was significantly degraded. Figure 18 shows the optical spots on the receiver plane for the (2 × 2)-clustered mode, where the power uniformity was 48.0%.

Table 3. Spot Size for the (2 × 2)-Clustered Mode at the Transmitter Plane

	Spot Size (μm)	
Row	Column 1	Column 2
1	24.1	21.8
	22.2	22.0
2	22.3	21.6
	22.4	23.5

The average spot size in the 2-clustered mode was 19.9 μm. This represented a slight increase compared with the spots at the power plane and transmitter plane. The uniformity of the spot size was measured to be 86.9%. Table 4 shows the measured spot sizes for the 2-clustered mode. The average spot size of the (2 × 2)-clustered spots was increased to 24.2 μm, and the spot-size uniformity was found to

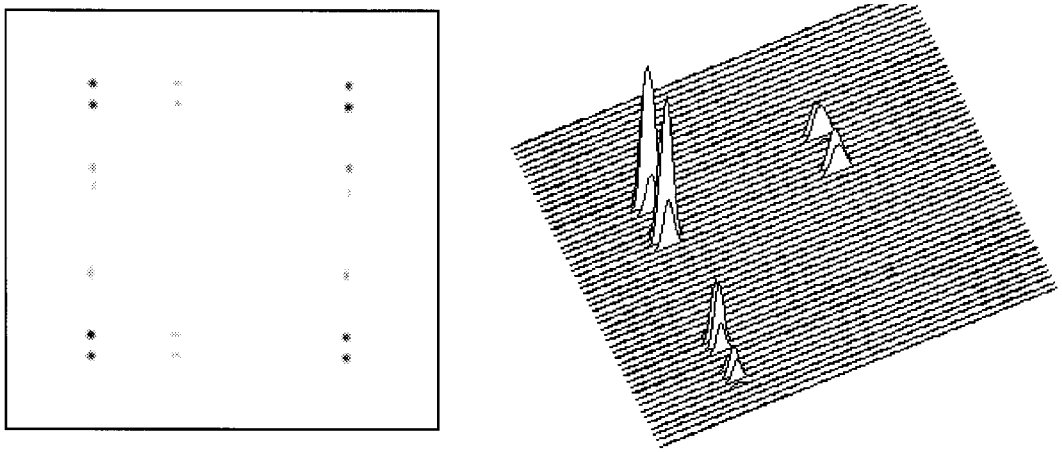

(a) (b)

Fig. 17. Optical spots at the receiver plane for the 2-clustered mode: (a) spot pattern and (b) 3-D plot of the upper-left portion of spots.

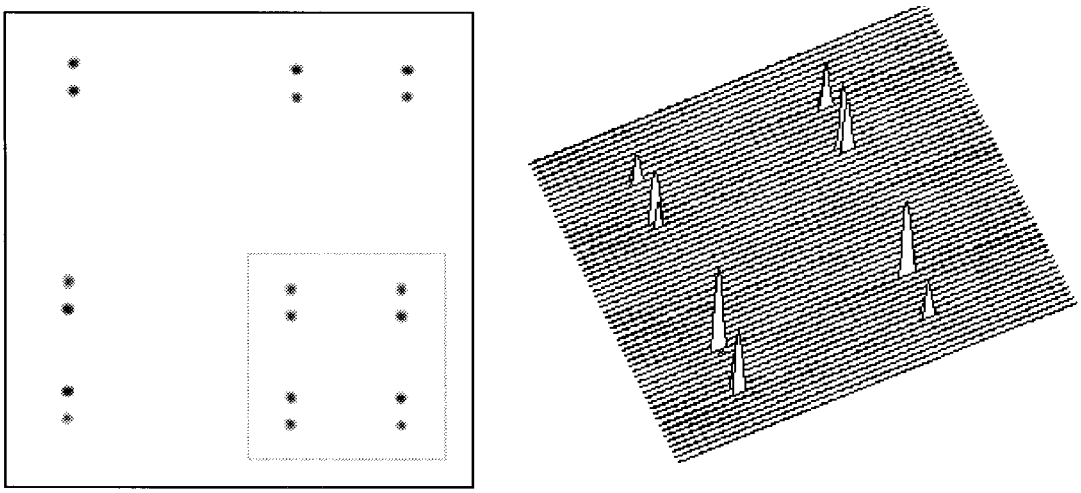

(a) (b)

Fig. 18. Optical spots at the receiver plane for the (2 × 2)-clustered mode: (a) spot pattern and (b) 3-D plot of the (2 × 2)-clustered spots shown in the box.

be 85.1%. In addition, the spots in the (2 × 2)-clustered mode showed strong astigmatism. Table 5 shows the measured spot sizes for the (2 × 2)-clustered mode.

Measurements were also performed by use of the FET-SEED transmitter array. It was found that the spots reflected from the active windows of a transmitter array had larger spot sizes. The spot size increased by approximately 18%. Moreover, the power and the spot size of the spot array reflected from a mirror at the transmitter plane were more uniform than those reflected from the transmitter windows. This was due in part to the lack of uniformity measured in the transmitter array.[8] In addition, the spots reflected from the mirror showed less astigmatism than did those from the transmitter windows. These results were caused by the clipping effects of the optical beams entering and exiting active windows, which had finite dimensions.

Finally, the magnification of the optical system was determined by measurement of the spot separations in the transmitter plane and receiver plane and comparison with the spot separation in the power plane. In both cases the measured separations were very close; thus the optical system had an almost 1:1 magnification.

The overall system performance was characterized by the data rates of connection channels. In the 2-clustered mode, data rates of 100 Mbits/s on each individual channel were achieved, and there was no significant optical cross talk when the system operated in this mode. In the (2 × 2)-clustered mode, the data rates for each channel were 25 Mbits/s. The lower data rates were due to the degradation of the quality of the optical beams at both the transmitter and receiver planes, since the optical system was not optimized to operate in this mode. The corresponding connection densities were 555 connections/cm^2 (277 channels/cm^2) for the 2-clustered mode and 2222 connections/cm^2 (1111 channels/cm^2) for the (2 × 2)-clustered mode, respectively. The significant increase of the connection density with window clustering provides a method for scaleability of free-space interconnects at the backplane level of an interconnection hierarchy.

Table 4. Spot Size for the 2-Clustered Mode at the Receiver Plane

	Spot Size (μm)	
Row	Column 1	Column 2
1	20.2	18.7
	20.9	20.9
2	19.7	20.3
	18.3	20.1

Table 5. Spot Size for the (2 × 2)-Clustered Mode at the Receiver Plane

	Spot Size (μm)	
Row	Column 1	Column 2
1	25.1	25.4
	23.2	24.8
2	23.4	22.4
	23.0	21.9

6. Conclusions

We have described the design and performance of a window-clustering microchannel free-space optical interconnect intended for optical backplane applications. The optical design, based on Gaussian beam propagation theory, was presented. Image mapping associated with a free-space optical interconnect was discussed. The prototype optical system was primarily designed to operate in the 2-clustered window mode but was also able to operate in the (2 × 2)-

clustered modes. In the 2-clustered window mode, the optical system achieved a date rate of 100 Mbits/s per channel. In the (2 × 2)-clustered mode, each data channel operated at 25 Mbits/s. Although the optical system was not optimized to operate in the (2 × 2)-clustered mode, it demonstrated that an optical system that applys a window-clustering scheme can have high channel density.

Optical system characterization for both modes of operation was performed and compared. In contrast to the general belief that it is necessary to sample a minimum of 2.15 periods for a BPG to have a good power uniformity across the array, sampling 1.66 periods in this prototype system provided a reasonably uniform spot array. The degradation of the data rate for each channel in the (2 × 2)-clustered mode was due to large clipping effects at the lenslets. The optimal system design for an optical interconnect requires a trade-off between channel density and the data rate of each individual channel. Further study should include developing a rigorous theory for the alignment tolerance of off-axis, strongly clipped, optical beams and an optimal optical system design that uses a better window-clustering scheme to realize a maximum overall data rate.

The authors gratefully acknowledge M. R. Taghizadeh of Heriot-Watt University for providing the diffractive lenslet arrays. This work was supported by the Canadian Institute for Telecommunication Research and the Nortel/NSERC Chair in Photonic Systems. In addition, D. V. Plant acknowledges support from NSERC (contract OPG0155159), Fonds pour la Formation de Chercheure et l'Aide á la Recherche (contract NC-1415), and the McGill University Graduate Faculty, and Y. Liu thanks D. Rolston for helping to prepare this manuscript.

References

1. J. W. Goodman, F. I. Leonberger, S. Y. Kung, and R. A. Athale, "Optical interconnects for VLSI systems," Proc. IEEE **72,** 850–875 (1984).
2. N. C. Craft and A. Y. Feldblum, "Optical interconnects based on arrays of surface-emitting lasers and lenslets," Appl. Opt. **31,** 1735–1739 (1992).
3. R. K. Kostuk, J. H. Yeh, and M. Fink, "Distributed optical data bus for board-level interconnects," Appl. Opt. **32,** 5010–5021 (1993).
4. T. Kato, F. Yuuki, K. Tanaka, H. Tanaka, H. Masuda, T. Tanoue, A. Oishi, K. Ito, K. Murakami, and T. Teraoka, "21 Gbits/s cm^2 throughput density two-dimensional array optical interconnection construction," Electron. Lett. **17,** 1722–1723 (1993).
5. D. V. Plant, B. Robertson, H. S. Hinton, W. M. Robertson, G. C. Boisset, N. H. Kim, Y. S. Liu, M. R. Otazo, D. R. Rolston, and A. Z. Shang, "An optical backplane demonstrator system based on FET-SEED smart pixel arrays and diffractive lenslet array," IEEE Photon. Technol. Lett. **7,** 1057–1059 (1995).
6. B. Robertson, G. C. Boisset, H. S. Hinton, Y. S. Liu, N. H. Kim, M. R. Otazo, D. Pavlasek, D. V. Plant, D. Rolston, and V. M. Robertson, "Design of a lenslet array based free-space optical backplane demonstrator," in *Proceedings of the International Conference on Optical Computing*, Vol. 139 of IOP Conference Proceedings (Institute of Physics, Bristol, UK, 1994), pp. 223–226.
7. D. Rolson, B. Robertson, D. V. Plant, and H. S. Hinton, "Analysis of a microchannel interconnect based on the clustering of smart-pixel-device windows," Appl. Opt. **35,** 1220–1233 (1996).
8. F. B. McCormick, F. A. P. Tooley, T. J. Cloonan, J. M. Sasian, H. S. Hinton, K. O. Merserau, and A. Y. Feldblum, "Optical interconnections using microlens arrays," Opt. Quantum Electron. **24,** S465–S477 (1992).
9. S. Tang, R. T. Chen, L. Garrett, D. Gerold, and M. M. Li, "Design limitations of highly parallel free-space optical interconnects based on arrays of vertical cavity surface-emitting laser diodes, microlenses, and photodetectors," J. Lightwave Technol. **12,** 1971–1975 (1994).
10. K. Hamanaka, "Optical bus interconnection system using Selfoc lenses," Opt. Lett. **16,** 1222–1224 (1991).
11. D. V. Plant, A. Z. Shang, M. R. Otazo, D. R. Rolston, B. Robertson, and H. S. Hinton, "Design, modeling, and characterization of FET-SEED smart pixel transceiver array for optical backplanes," J. Quantum Electron. (to be published).
12. A. L. Lentine, L. M. F. Chirovsky, L. A. D'Asaro, E. J. Laskowski, S. S. Pei, M. W. Focht, J. M. Freund, G. D. Guth, R. E. Leibenguth, L. E. Smith, and T. K. Woodward, "Field-effect-transistor self-electrooptic-effect-device (FET-SEED) electrically addressed differential modulator array," Appl. Opt. **33,** 2849–2855 (1994).
13. K. Tanaka and O. Kanzaki, "Focus of a diffracted Gaussian beam through a finite aperture lens: experimental and numerical investigations," Appl. Opt. **26,** 390–395 (1987).
14. F. B. McCormick, F. A. P. Tooley, J. L. Brubaker, J. M. Sasian, T. J. Cloonan, A. L. Lentine, S. J. Hinterlong, and M. J. Herron, "Optomechanics of a free-space switch: the system," in *Optomechanics and Dimensional Stability*, R. A. Paquin and D. Vukobratoviich, eds., Proc. SPIE **1720,** 553–572 (1992).
15. P. Belland and J. P. Crenn, "Changes in the characteristics of a Gaussian beam weakly diffracted by a circular aperture," Appl. Opt. **21,** 522–527 (1982).
16. S. M. Prince, C. P. Beauchamp, and F. A. P. Tooley, "Tolerancing of arrays of microlens relays: a case study," J. Europ. Opt. Soc. Part A **3,** 151–156 (1994).
17. W. C. Sweatt, "Mathematical equivalence between a holographic optical element and an ultra-high index lens," J. Opt. Soc. Am. **69,** 486–487 (1979).
18. D. C. Sinclair, "Designing diffractive optics using the Sweatt model," Sinclair Opt. Design Notes **1** (1) (1990).
19. J. N. Mait, "Design of binary-phase and multiphase Fourier gratings for array generation," J. Opt. Soc. Am. A **7,** 1514–1528 (1990).
20. M. P. Dames, R. J. Dowling, P. McKee, and D. Wood, "Efficient optical elements to generate intensity weighted spot arrays: design and fabrication," Appl. Opt. **30,** 2685–2691 (1991).
21. F. B. McCormick, "Generation of large spot arrays from a single laser beam by multiple imaging with binary phase gratings," Opt. Eng. **28,** 299–304 (1989).
22. F. B. McCormick, "Free-space interconnection techniques," in *Photonics in Switching*, J. E. Midwinter, ed. (Academic, New York, 1993), pp. 185–189.
23. J. Jahns and S. J. Walker, "Two-dimensional array of diffractive microlenses fabricated by thin film deposition," App. Opt. **29,** 931–936 (1990).
24. A. E. Siegman, *Laser* (University Science, Mill Valley, Calif., 1986), Chap. 17.